processes

MDPI

Article

Anticancer Activity of Anti-Tubercular Compound(s) Designed on Pyrrolyl Benzohydrazine Scaffolds: A Repurposing Study

Turki Al Hagbani [1], Afrasim Moin [1], Talib Hussain [2], N. Vishal Gupta [3], Farhan Alshammari [1], Syed Mohd Danish Rizvi [1,*] and Sheshagiri Dixit [4,*]

[1] Department of Pharmaceutics, College of Pharmacy, University of Ha'il, Ha'il 81442, Saudi Arabia; t.alhagbani@uoh.edu.sa (T.A.H.); a.moinuddin@uoh.edu.sa (A.M.); frh.alshammari@uoh.edu.sa (F.A.)
[2] Department of Pharmacology and Toxicology, College of Pharmacy, University of Ha'il, Ha'il 81442, Saudi Arabia; md.talib@uoh.edu.sa
[3] Department of Pharmaceutics, JSS College of Pharmacy, JSS Academy of Higher Education and Research, Mysore 570015, India; vishalkumargupta@jssuni.edu.in
[4] Department of Pharmaceutical Chemistry, JSS College of Pharmacy, JSS Academy of Higher Education and Research, Mysore 570015, India
* Correspondence: sm.danish@uoh.edu.sa (S.M.D.R.); sheshagiridixit@jssuni.edu.in (S.D.)

Abstract: The present study explored anti-tubercular pyrrole derivatives against cancer targets using different in silico and in vitro approaches. Initially, nineteen anti-tubercular pyrrolyl benzohydrazide derivatives were screened against a potent cancer target PLK1 using an AutoDock Vina approach. Out of the nineteen derivatives, the two most potent derivatives **C8** [N′-(4-(1H-pyrrol-1-yl) benzoyl)-3-chlorobenzohydrazide] and **C18** [N′-(4-(1H-pyrrol-1-yl) benzoyl)-4-nitrobenzohydrazide], were subjected to molecular simulation analysis for a 100 ns trajectory. Further, these two derivatives were tested against A549, MCF-7, and HepG2 cell lines using an MTT proliferation assay. Apoptotic cell cycle and DAPI assays were also performed for **C8** on A549 cell lines. Molecular dynamic analysis revealed that the stability of the **C8**–PLK1 protein complex during the 100 ns trajectory run was better than that of the **C18**–PLK1 protein complex. In addition, **C8** showed lower IC_{50} values against the tested cell lines, in comparison to **C18**. Thus, **C8** was selected for cell cycle, apoptosis, and DAPI analysis. Interestingly, **C8** resulted in the significant cell cycle arrest of A549 cells at the G2/M phase, and annexin V-FITC/PI showed a significant increase (from 6.27% to 60.52%) in the percentage of apoptotic A549 cells. The present findings suggest that the anti-tubercular compound (**C8**) could be translated into a potent repurposed candidate against lung cancer. Nevertheless, in vivo assessment is necessary to further confirm the outcome and its clinical translation.

Keywords: anti-tubercular; anti-cancer; drug repurposing; PLK1; pyrrolyl benzohydrazide derivative

Citation: Hagbani, T.A.; Moin, A.; Hussain, T.; Gupta, N.V.; Alshammari, F.; Rizvi, S.M.D.; Dixit, S. Anticancer Activity of Anti-Tubercular Compound(s) Designed on Pyrrolyl Benzohydrazine Scaffolds: A Repurposing Study. *Processes* **2023**, *11*, 1889. https://doi.org/10.3390/pr11071889

Academic Editors: Alina Bora and Luminita Crisan

Received: 24 April 2023
Revised: 1 June 2023
Accepted: 19 June 2023
Published: 23 June 2023

1. Introduction

Onco-therapy is a major concern for the scientific community due to the multifactorial features of cancer disease. According to a report, every year, 50 billion dollars are spent on cancer research and development to develop new onco-drug candidates [1], but the WHO reported 10 million cancer-associated deaths worldwide in the year 2020 [2]. In addition, the cancer-linked deaths are increasing at an alarming rate with time [3]. Thus, solutions are urgently warranted to cope with the current grave situation. However, drug repurposing has opened a new avenue for effective cancer treatment [4,5]. Repurposing can reduce the developmental cost, timeline, processing, and approval requirements. In other words, repurposing can overcome the bottlenecks associated with cancer drug development. Several reports have suggested that anti-tubercular agents could be repurposed for cancer therapy [6–11]. Bedaquiline, isoniazid, ethionamide, prothionamide, and thioacetazone are some examples of anti-tubercular drugs/agents that were successfully repurposed

for cancer treatment. These findings prompted us to explore anti-tubercular pyrrolyl benzohydrazide derivatives as anti-cancer agents.

Earlier, in the year 2017, several pyrrolyl benzohydrazide derivatives were synthesized and tested for anti-tubercular potential [12]. In the present study, the same pyrrolyl benzohydrazide derivatives [12] were used, to obtain deeper insight into their anticancer potential, with the reason being the well-reported potent anticancer activity of pyrrole analogs and benzohydrazide derivatives [13,14]. The pyrrole scaffold has its due relevance while designing important medicinal drugs. Pyrrole has a typical aromatic nitrogen-containing heterocycle, and the existence of nitrogen atom significantly improves the polarity of the pyrrole analogs [15]. In addition, the pyrrole ring is an important component of plant chlorophyll and animal vitamin B12, hemin, and myoglobin [14]. Moreover, their derivatives have shown a valuable pharmacological profile and potent anticancer activities in different investigations [14–19]. In fact, some of marketed drugs already have pyrrole moieties in them to enhance their potency [14,15]. On the other hand, there are a plethora of reports suggesting the potent anticancer activities of benzohydrazide derivatives [13,20–25]. Benzohydrazide derivatives might follow different mechanisms of action against different cancer cells; they could act as inhibitors of VEGFR-2 [21], lysine-specific histone demethylase 1A [22], tubulin polymerization [23], Bcl-2/Bcl-xL [24], and CD44 [25]. However, reports [13,20–25] clearly suggest that benzohydrazide derivatives could be applied for a variety of cancer cells. Taking into consideration the pharmacological and anticancer activities of benzohydrazide and pyrrole derivatives, the compounds derived from them via a hybridization approach [12] were used in the present study to assess their anticancer potential.

Prior to wet lab investigations, nineteen anti-tubercular pyrrolyl benzohydrazide derivatives were screened through computational analysis to select the best compounds out of them. This computational study was performed using molecular docking interaction analysis and molecular dynamics. Further, the selected compounds (**C8** [N′-(4-(1H-pyrrol-1-yl) benzoyl)-3-chlorobenzohydrazide] and **C18** [N′-(4-(1H-pyrrol-1-yl) benzoyl)-4-nitrobenzohydrazide]) were investigated using different cell lines i.e., A549, MCF-7, and HepG2. Moreover, compound **C8** was further subjected to cell cycle, apoptosis, and DAPI analysis using A549 cells. The repurposing of anti-tubercular compounds into anticancer drugs, as well as against lung cancer, seems to be an appealing approach. It is like hitting two birds with one stone, as tuberculosis is one of the strong risk factors of lung cancer.

2. Materials and Methods

2.1. Synthesis of Pyrrolyl Benzohydrazide Derivatives

Nineteen pyrrolyl benzohydrazide derivatives were selected from the prior study [12] conducted for anti-tuberculosis potential. In the study [12], the Pall–Knorr pyrrole synthesis approach, as shown in Scheme 1, was used to synthesize the derivatives. The most active compound, **C8** [N′-(4-(1H-pyrrol-1-yl) benzoyl)-3-chlorobenzohydrazide], was synthesized by using ethyl 4-amino benzoate as a starting material, which was refluxed with 2,5-dimethoxy tetrahydrofuran at 150–160 °C for 45 min. The formed pyrrolyl ester was hydrazide by using hydrazine hydrate, and the formed hydrazide was stirred at room temperature for 24–30 h with 3-chlorobenzaldehyde with the help of HBTU [2-(1H-benzotriazole-1-yl)-1,1,3,3-tetramethyl uronium hexa fluorophosphate] and DIEA (diisopropyl ethylamine), a coupling agent and a catalyst to form **C8**.

2.2. Dry Lab Investigations

2.2.1. Ligand Preparation for Molecular Docking

Three dimensional structures of these compounds were prepared using ChemDraw software and saved in .pdb format. Further, all the ligands, including the positive control (BI2536; DrugBank ID: DB16107) and native ligand (DrugBank ID: DB07186), were converted into .pdbqt format using the OpenBabel tool [26].

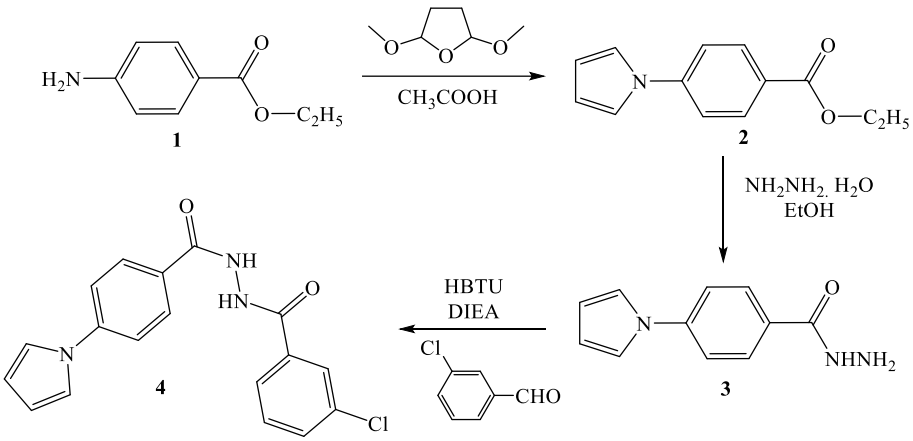

Scheme 1. Synthesis route of pyrrolyl benzohydrazide derivatives.

2.2.2. Target Preparation for Molecular Docking

The three-dimensional structure of the target protein PLK1 (PDBID: 2OWB) was retrieved from the Protein Data Bank database in .pdb format. Further, it was prepared for docking via the AutoDock 4.2 tool [27], which included the addition of polar hydrogen, Kollman charges, and solvation parameters. Moreover, the target protein was converted and saved in .pdbqt format.

2.2.3. Molecular Docking Interaction Study

AutoDock Vina was applied for molecular docking of all the ligands with the PLK1 target protein [28]. Prior to docking, grid co-ordinates were set on the specified active kinase domain of the PLK1 protein [29]. Grid center coordinates were kept as x = 0.069, y = 23.58, and z = 66.741, and the grid box was set at 40 × 40 × 40. The results showed affinity in terms of kcal/mol, and the algorithm divided the results in descending order of the 10 modes. Further, the Pymol tool was used to save the complex of best conformation based on the affinity results for each docked structure. Moreover, the Discovery Studio Visualization tool was used to analyze and visualize the complex in more detail.

2.2.4. Molecular Dynamics (MD) Simulation Study

Out of nineteen pyrrolyl benzohydrazide derivatives, two derivatives, i.e., **C8** [N′-(4-(1H-pyrrol-1-yl)benzoyl)-3-chlorobenzohydrazide] and **C18** [N′-(4-(1H-pyrrol-1-yl)benzoyl)-4-nitrobenzohydrazide] were screened out through molecular docking interactions, and MD simulations were performed on them to obtain better insight into **C8** and **C18** interactions with PLK1 under solvated states with respect to time. The GROMACS 5.1.5 [30] platform applied with a CHARMM27 [31] forcefield was used for executing simulation runs on PLK1 in an undocked native state and docked (with **C8** and **C18**) complex state. Ligand **C8** and **C18** topology files were created through the SwissParam server by applying all atoms of the CHARMM force field [32]. A cut-off distance of 1 nm was set for estimating Van der Waal and columbic interactions. However, neutrality of the system was maintained by adding counter ions, and the TIP3P water model was used to solvate the system. Periodic boundary conditions were applied by keeping a distance of 1 to 1.5 nm from the wall for the simulation run [33]. Energy minimization was performed with a 1000 kJ/mol/nm tolerance by applying the steepest descent algorithm, and position restrains were applied on the complex to equilibrate the system. NPT and NVT ensembles were used for 200 ps at 1 bar of pressure and a temperature of 300 K. Maxwell distribution was used to generate primary velocities, and a 0.1 ps coupling constant was used for velocity rescaling. The Parrinello–Rahman algorithm was used for temperature–pressure coupling with a 2 ps coupling constant. The system after equilibration was subjected to a 100 ns simulation run with a 2 fs time-step integration [34]. After each 500 steps, the trajectory was saved and analyzed using XMGRACE-5.1.22 and GROMACS analysis tools.

2.3. Wet Lab Investigations

2.3.1. Materials

The cancer cell lines (breast cancer MCF-7, lung cancer A549, and liver cancer HepG2) were procured from NCCS, India. Chemicals pertinent to cell culture were obtained from BD Biosciences (Franklin Lakes, NJ, USA). Solvents, chemicals, and MTT dye were purchased from HiMedia (Thane, India), whereas doxorubicin (standard drug) was procured from Sigma-Aldrich.

2.3.2. Cell Culture

A549, MCF-7, and HepG2 cell lines were cultured in DMEM medium, supplemented with 100 IU/mL penicillin, 100 µg/mL streptomycin, and 10% inactivated fetal bovine serum, in 5% CO_2 saturated conditions at 37 °C until confluence occurred. However, the viability of the cells was examined periodically.

2.3.3. Stock Solution of Tested Compounds

The stock solutions (20 mM) of pyrrolyl benzohydrazide derivatives and the positive control doxorubicin were prepared using a DMSO solvent.

2.3.4. Cytotoxic In Vitro MTT Assay

An MTT assay was applied to calculate the cytotoxic concentration of compounds (**C8** and **C18**) [35]. For this, 100 µL of cells (50,000 cells) was added to each well of a microtiter plate and treated with a medium containing 0.78, 1.56, 3.125, 6.25, 12.5, 25, 50, and 100 µM concentrations of **C8**, **C18**, and doxorubicin. Further, the plates were kept in an incubator (with 5% CO_2) for 24 h at 37 °C. After that, MTT dye, 20 µL from the stock (5 mg MTT in 1 mL PBS), was inoculated in each well and kept in an incubator under the same condition again for 4 h. The supernatant after treatment was collected and centrifuged, and DMSO (200 µL) was added to the pellet. Furthermore, this solution was added to its respective well, and formazan crystals were dissolved by shaking the plates. A microplate reader was used to measure the absorbance at 590 nm. The following formula was applied to calculate the % inhibition of growth for each cell line:

$$\%\text{Inhibition} = 100 - (\text{OD of Sample} \div \text{OD of Control}) \times 100$$
$$\%\text{Cell Viability} = 100 - \%\text{Inhibition}$$

2.3.5. Cell Cycle Analysis

A 6-well plate with a density of 2 × 105 cells/2 mL was incubated in a CO_2 incubator, which was kept overnight at 37 °C for 24 h. The cells educed were treated with **C8** (10 µM) in a 2 mL culture medium and incubated for 24 h. The medium was given a PBS wash, trypsinized, and harvested into a 5 mL storage vial. After 2 steps of PBS washes, the cells were fixed and permeabilized in 1 mL of pre-chilled 70% ethanol, added drop-wise with continuous stirring, to avoid the clumping of cells. The cells were incubated for 30 min in a −20 °C freezer. The cells educed were obtained and washed with PBS. Further, the cells were stained using 400 µL Propidium Iodide/RNase staining buffer that stains the DNA [36]. Again, the cells were incubated for 15 to 20 min at room temperature in the dark. The samples were analyzed using flow cytometry. A minimum of 10,000 cells was counted for each group.

2.3.6. Cell Apoptosis Assay

An apoptosis study was performed to understand Annexin V/PI expression using the A549 cell line [37]. A 6-well plate with a density of 0.5 × 106 cells/2 mL was incubated in a CO_2 incubator and kept overnight at 37 °C for 24 h. The cells educed were treated with **C8** (10 µM) in a 2 mL culture medium and incubated for 24 h. The medium was given a PBS wash; further, 200 µL of the trypsin–EDTA solution was added and again incubated for a few minutes. Subsequently, the cells were harvested in 12 × 75 mm polystyrene tubes

with an additional 2 mL of culture media. The tubes were centrifuged for 5 min at 300× *g* at 25 °C. Later, the supernatant layer was decanted. Again, a PBS wash was given, and a further 5 µL of FITC Annexin V was added. Gentle stirring of the cells was performed, and they were incubated in the dark for 15 min at room temperature (25 °C). Then, 5 mL of PI and 400 µL of 1X Annexin Binding Buffer was added to each tube and stirred gently. The sample was analyzed using flow cytometry.

2.3.7. DAPI Assay

A 96-well glass-bottom plate with a density of 1 × 104 cells/200 µL was incubated in a CO_2 incubator and kept overnight at 37 °C for 24 h. The cells educed were treated with **C8** (10 mM) in 200 µL of culture medium and incubated for 24 h. The medium was given a PBS wash. Further, the cells were stained by adding 200 µL of DAPI staining solution for 10 min in the dark [38]. The cells were observed under a ZEISS, LSM 880 Fluorescence live-cell Imaging System (Confocal Microscopy, Jena, Germany) with a filter cube, with excitation at 358 nm and emission at 461 nm for DAPI.

2.3.8. Statistical Analysis

Statistical analysis was performed using one-way ANOVA and a Student *t*-test using Graph Pad Prism version 8.

3. Results and Discussion

De novo drug development for cancer is a tedious and multi-step process. This is due to the high heterogenicity and complexity associated with the cancer disease. In fact, cancer drug development is a time-, resource-, and labor- intensive job, and it has been observed that only a few drugs could pass the initial phases of the clinical trial after spending too much effort. Hence, drug repurposing has come up as a savior, wherein established drugs are proposed for new avenues in the field of cancer medication [5,39]. Even big pharma industries are investing in drug repurposing, and the drug repurposing market size has reached 25.2 billion US$ in the year 2021 [40]. Thus, this current research study attempted to assess the repurposing potential of anti-TB pyrrolyl benzohydrazide derivatives [12] (Figure 1) as anti-cancer agents.

3.1. Molecular Interaction of Pyrrolyl Benzohydrazide Derivatives with PLK1

Polo Like Kinase 1 is a well-established cancer target [41], and its overexpression is observed in several cancer cells, such as lung, pancreatic, ovarian, prostate, colorectal, and breast. Importantly, its expression is very low in normal cells, while it significantly increases in cancer cells [41,42]. In addition, PLK1 inhibition has been considered one of the potent strategies against cancer [43–45]. Thus, in the present study, nineteen pyrrolyl benzohydrazide derivatives (Table 1) that have been reported for anti-tuberculosis potential [12] were screened against the PLK1 enzyme.

Table 1. Docking results of pyrrolyl benzohydrazide derivative, control, and native ligand interactions with the target PLK1.

Compound Code	Name of Compound	Binding Affinity
C1	N′-(4-(1H-pyrrol-1-yl)benzoyl)-2,4-dichlorobenzohydrazide	−9 kcal/mol
C2	N′-(4-(1H-pyrrol-1-yl)benzoyl)-2-aminobenzohydrazide	−8.8 kcal/mol
C3	N′-(4-(1H-pyrrol-1-yl)benzoyl)-2-bromobenzohydrazide	−8.9 kcal/mol
C4	N′-(4-(1H-pyrrol-1-yl)benzoyl)-2-chlorobenzohydrazide	−9 kcal/mol

Table 1. *Cont.*

Compound Code	Name of Compound	Binding Affinity
C5	N′-(4-(1H-pyrrol-1-yl)benzoyl)-2-methylbenzohydrazide	−8.9 kcal/mol
C6	N′-(4-(1H-pyrrol-1-yl)benzoyl)-3-acetylbenzohydrazide	−9 kcal/mol
C7	N′-(4-(1H-pyrrol-1-yl)benzoyl)-3-aminobenzohydrazide	−7.8 kcal/mol
C8	N′-(4-(1H-pyrrol-1-yl)benzoyl)-3-chlorobenzohydrazide	−9.7 kcal/mol
C9	N′-(4-(1H-pyrrol-1-yl)benzoyl)-3-methylbenzohydrazide	−9.1 kcal/mol
C10	N′-(4-(1H-pyrrol-1-yl)benzoyl)-3-nitrobenzohydrazide	−9 kcal/mol
C11	N′-(4-(1H-pyrrol-1-yl)benzoyl)-4-aminobenzohydrazide	−8.8 kcal/mol
C12	N′-(4-(1H-pyrrol-1-yl)benzoyl)-4-bromobenzohydrazide	−8.9 kcal/mol
C13	N′-(4-(1H-pyrrol-1-yl)benzoyl)-4-chlorobenzohydrazide	−9 kcal/mol
C14	N′-(4-(1H-pyrrol-1-yl)benzoyl)-4-fluorobenzohydrazide	−8.8 kcal/mol
C15	N′-(4-(1H-pyrrol-1-yl)benzoyl)-4-hydroxybenzohydrazide	−8 kcal/mol
C16	N′-(4-(1H-pyrrol-1-yl)benzoyl)-4-methoxybenzohydrazide	−8.9 kcal/mol
C17	N′-(4-(1H-pyrrol-1-yl)benzoyl)-4-methylbenzohydrazide	−8.7 kcal/mol
C18	N′-(4-(1H-pyrrol-1-yl)benzoyl)-4-nitrobenzohydrazide	−9.6 kcal/mol
C19	N′-benzoyl-4-(1H-pyrrol-1-yl)benzohydrazide	−9 kcal/mol
Control (BI2536)	4-{[(7R)-8-cyclopentyl-7-ethyl-5-methyl-6-oxo-5,6,7,8-tetrahydropteridin-2-yl]amino}-3-methoxy-N-(1-methylpiperidin-4-yl)benzamide	−9.3 kcal/mol
Native Ligand	4-(4-methylpiperazin-1-yl)-N-{5-[2-(thiophen-2-yl)acetyl]-1H,5H-pyrrolo[3,4-c]pyrazol-3-yl}benzamide	−8.6 kcal/mol

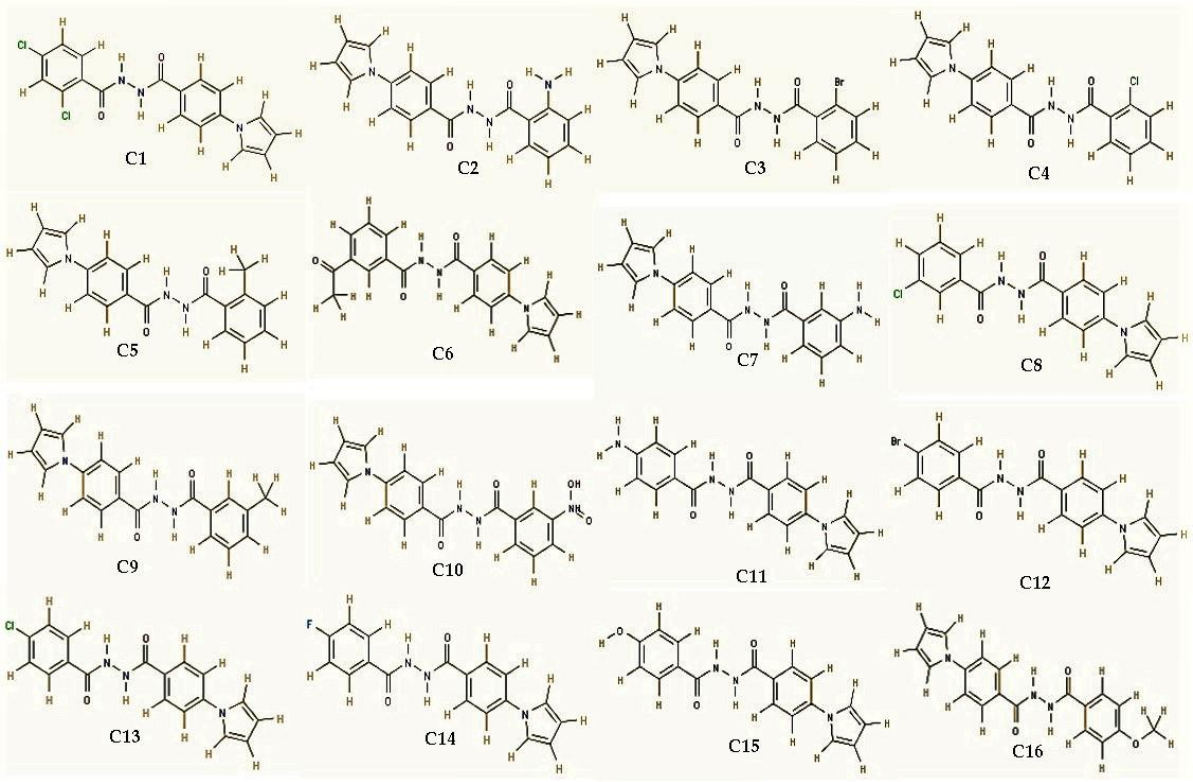

Figure 1. *Cont.*

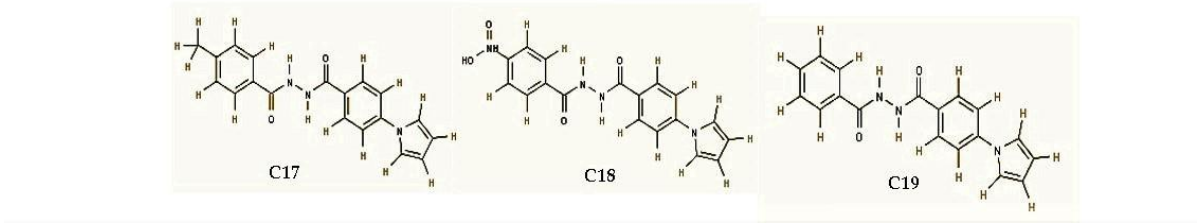

Figure 1. Structures of nineteen pyrrolyl benzohydrazide derivatives used in the present study.

The screening results depicted that N′-(4-(1H-pyrrol-1-yl)benzoyl)-3-chlorobenzohydrazide (**C8**) and N′-(4-(1H-pyrrol-1-yl)benzoyl)-4-nitrobenzohydrazide (**C18**) were the most potent among the nineteen tested derivatives against PLK1 (Table 1). Both **C8** and **C18** showed significant interactions with the 'kinase domain' of PLK1. The Gibbs free energy (ΔG) of the '**C8**-PLK1 interaction' was −9.7 kcal/mol, whereas ΔG of the '**C18**-PLK1 interaction' was −9.6 kcal/mol. To obtain a deeper insight into **C8** and **C18** interactions, the results were compared with the interactions of the positive control (BI2536) with PLK1 (Figure 2; Table 2). A redocking native ligand experiment was performed to validate the protocol, wherein the re-docked native ligand bound to the same vicinity of the PLK1 'active site' as the native ligand [46]. A superimposition image (Figure 2b) established the protocol standardization; in addition, all of **C8**, **C18**, and the positive control were also bound to the same domain of PLK1 (Figure 2a). However, the ΔG values (Table 2) suggested that **C8** and **C18** showed better interactions with PLK1 than the positive control (−9.3 kcal/mol) and native ligand (−8.6 kcal/mol). Insights into amino acids involved in the individual ligand interactions with PLK1 were shown through LigPlot analysis (Figure 2d). LigPlot analysis for both **C8** (Figure 2(d1)) and **C18** (Figure 2(d2)) showed that 13 amino acid residues, (i.e., Leu59, Cys67, Ala80, Val114, Leu130, Glu131, Leu132, Cys133, Arg134, Arg136, Phe183, Gly193, Asp194) interacted with the 'kinase domain' of PLK1. Here, Cys133 interacted through strong hydrogen bonding, while other amino acids showed hydrophobic interactions. However, the positive control (BI2536) displayed strong hydrogen bonding with Lys82, involving a total of 10 amino acid residues of PLK1 during the interaction (Figure 2(d3)). Strong hydrogen bonding interactions of **C8** and **C18** with the Cys133 amino acid residue of PLK1 (Figure 2(d1,d2)) have their due relevance, as Cys133 serves as a crucial part of the ATP-binding pocket, and it is considered a novel covalent site of PLK1 for drug discovery [41,47]. In addition, Shakil et al. [41] reported that Leu59, Cys67, Leu130, Cys133, Arg136, and Phe183 played an important role in PLK1 binding with different inhibitors. In fact, Leu132 formed the hinge region, and Cys67 and Phe183 configured the top/bottom of the ATP binding pocket. Importantly, both compounds **C8** and **C18** became associated with all these critical amino acid residues of the PLK1 ATP-binding pocket. The activation loop of PLK1 (2OWB) consists of Val210 (i.e., Thr210 a primary phosphorylation site of wild-type Plk1) and Ser137 (a secondary phosphorylation site). Neither of these two amino acids showed an interaction with **C8** and **C18**. However, to confirm their dynamic behavior with respect to time, both of these compounds were further subjected to molecular dynamics analysis.

Table 2. Interacting amino acids and binding energy of substrate docked with the active site of PLK1.

Ligands	Binding Energy	Interacting Amino Acids of PLK1
C8	−9.7 kcal/mol	Leu59, Cys67, Ala80, Val114, Leu130, Glu131, Leu132, **Cys133** *, Arg134, Arg136, Phe183, Gly193, Asp194
C18	−9.6 kcal/mol	Leu59, Cys67, Ala80, Val114, Leu130, Glu131, Leu132, **Cys133** *, Arg134, Arg136, Phe183, Gly193, Asp194

Table 2. *Cont.*

Ligands	Binding Energy	Interacting Amino Acids of PLK1
Positive control (BI2536)	−9.3 kcal/mol	Gly60, Lys61, Gly62, Gly63, Phe64, **Lys82** *, Val84, Lys97, Phe183, Asp194
Redocked Native ligand (DB07186)	−8.6 kcal/mol	Lys61, Gly62, Gly63, Phe64, Cys67, Lys82, Val114, Glu131, Cys133, Arg136, Phe183, Asp194, Gly 196

* Hydrogen bonded amino acids are represented in bold.

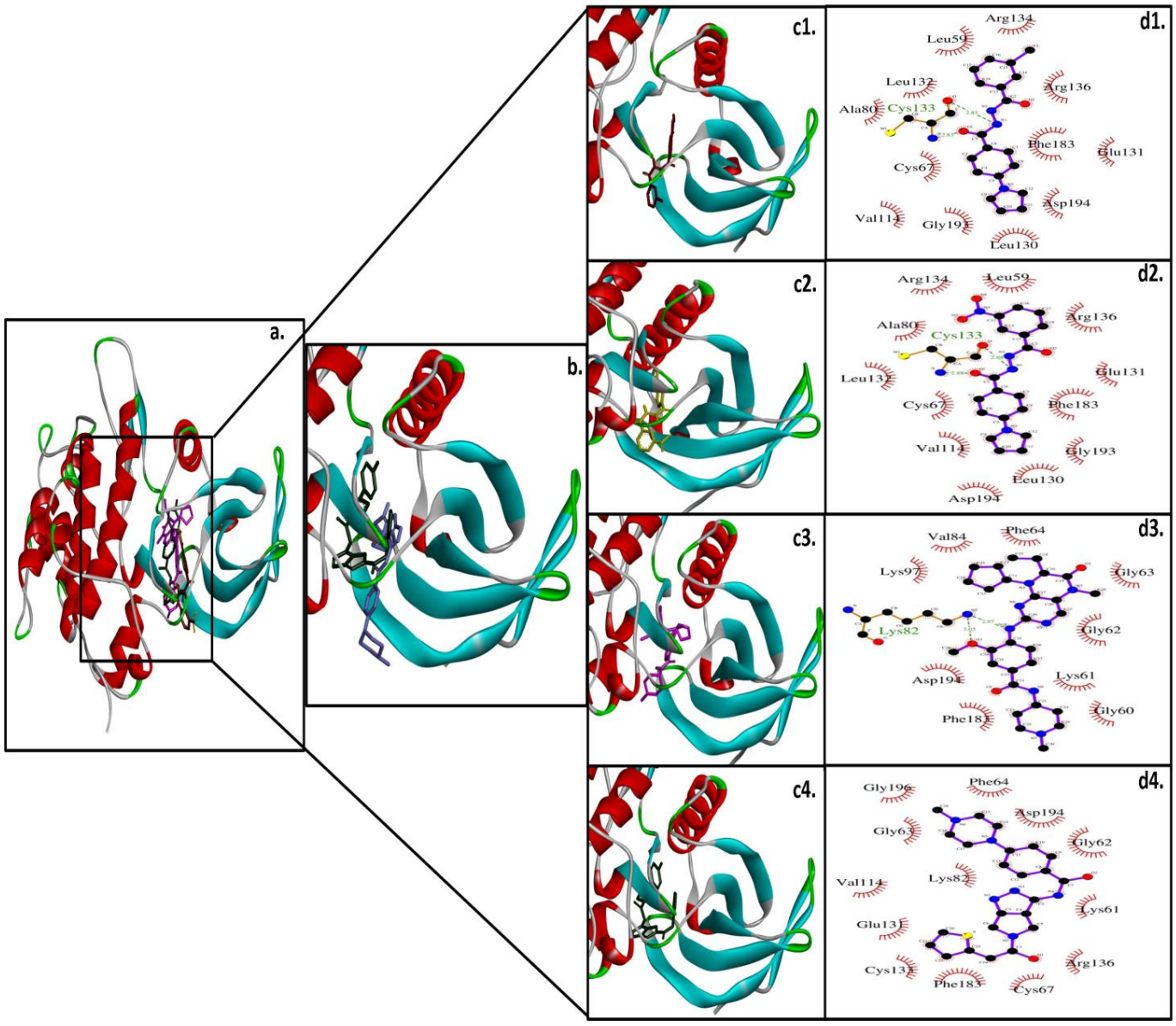

Figure 2. Ligand-docked active site images of PLK1 (PDB ID: 2OWB). (**a**) All the docked ligands (**C8**: red color; **C18**: yellow color; positive control (BI2536): magenta color; native ligand (DB07186): green color) in the catalytic active site of PLK1. (**b**) Enlarged overlay image of native ligand and redocked native ligand. (**c**) Enlarged image of (**c1**) **C8** docking, (**c2**) **C18** docking, (**c3**) BI2536 docking, and (**c4**) DB07186 docking. (**d**) Molecular interaction analysis of all the compounds ((**d1**): **C8**; (**d2**): **C18**; (**d3**): BI2536; (**d4**): DB07186) with PLK1 amino acid residues.

3.2. Molecular Dynamic (MD) Analysis of **C8** and **C18** with PLK1

The dynamic behavior of '**C8**-PLK1' and '**C18**-PLK1' complexes, under solvated conditions, was studied through an MD simulation/mimicking study with respect to time. The best docking pose for each complex was mapped for stability under a mimicable environment. The outcomes of the mimicking study, with various constraints helping us to understand the binding mode and stability, were reported in terms of the solvent accessible surface area (SASA), radius of gyration (R_g), number of hydrogen bonds, root mean square deviation (RMSD), and root mean square fluctuation (RMSF). All these parameters were mapped during the mimicking study time, and deviation of the secondary structure pattern between the protein and their complexes was measured.

Three mimicking studies with the protein (PLK1) alone (black color) and its complex with ligand **C8** (red color) and **C18** (green color) were executed for a 100 ns time duration. From the RMSD plot (Figure 3a), it was observed that the **C8**–PLK1 complex, after initial fluctuation, reached equilibrium at approximately 10 ns of time. After that, the complex displayed a constant trajectory with marginal deviation of ~0.1 nm, indicating that the structural stability of the protein was preserved while in complex with **C8**. Results also suggested that the unbound protein (PLK1 alone) also reached equilibrium after an initial fluctuation, and it showed a similar pattern of stable trajectory as **C8** bound PLK1. On the other hand, **C18**-bound PLK1 was stable until 80 ns and started fluctuating in the range of ~0.3 nm until 90 ns. However, it also became stable at the end after this 10 ns fluctuation. The Rg plot (Figure 3b) showed that all the entries (including the innate protein (PLK1) and its complex forms with **C8** and **C18**) exhibited a similar pattern of Rg during the entire simulation time with minimal (0.05 nm) variation in different distance ranges. Hydrogen bonding between the ligand and protein complex was evaluated, which in turn forecasted the focalization of the ligand into the binding cavity of the protein. All the intermolecular H-bonds among ligands and the protein were studied and plotted accordingly (Figure 3c). From the plot, it is clear that the number of H-bonds involved in the simulation runs fluctuated over time, but most strong H-bonds remained intact throughout the study time. The disappearance and then reappearance of a few H-bonds indicate the vital nature of the ligand inside the binding cavity. The solvent accessible surface area (SASA) determined the area surrounding the hydrophobic core developed between the protein–ligand complexes (Figure 3d). Reliable SASA values were obtained with a fluctuation of 10 nm^2 area for PLK1 and the **C8**–PLK1 complex, whereas more fluctuations of a 15 nm^2 area were observed in case of the **C18**–PLK1 complex. The SASA plots for PLK1 and **C8**–PLK1 almost overlapped with each other; however, **C18**–PLK1 complexes showed no overlap during 25 ns to 60 ns and after 90 ns until the end of the simulation run. The residue-wise variations were observed in the RMSF plot (Figure 3e,f), wherein the potentially interacting amino acids stiffened in the complex forms (**C8**–PLK1 and **C18**–PLK1) in comparison to the normal protein state (PLK1).

In addition, dynamic behavior of the 'PLK1-BI2536 (control)' complex under solvated conditions were also studied through an MD simulation study with respect to time (Figure S1 Supplementary Materials). From the RMSD plot (Figure S1a), it was observed that the BI2536–PLK1 complex, after initial fluctuation, reached equilibrium at approximately 10 ns of time. After that, the complex displayed constant trajectory with marginal deviation of ~0.09 nm, indicating that the structural stability of the protein was preserved while in complex with BI-2536. On the other hand, the Rg plot (Figure S1b) showed that the gyration of the protein–ligand complex (PLK1–BI2536) exhibited a similar pattern of Rg during the entire simulation time with minimal (0.025 nm) variation in different distance ranges after initial fluctuations. From the hydrogen bonding plot (Figure S1c), it was clear that the number of H-bonds involved in the simulation runs fluctuated over time but most strong H-bonds were intact during the study time. Furthermore, reliable SASA values (Figure S1d) were obtained with an initial fluctuation of a 15 nm^2 area for the PLK1–BI2536 complex up to 10 ns; however, minimal fluctuations of a 10 nm^2 area were observed after 10 ns until the end of the simulation run. The residue-wise variations were observed in the

RMSF plot (Figure S1e), where potentially interacting amino acids became stiffened in the complex form (PLK1-BI2536) similar to PLK1–**C8** and PLK1–**C18** complexes. In fact, from the findings of MD simulation results of PLK1–BI2536, it could be inferred that an almost similar pattern was observed for the control compound (BI2536) as in the case of the tested compounds (**C8** and **C18**).

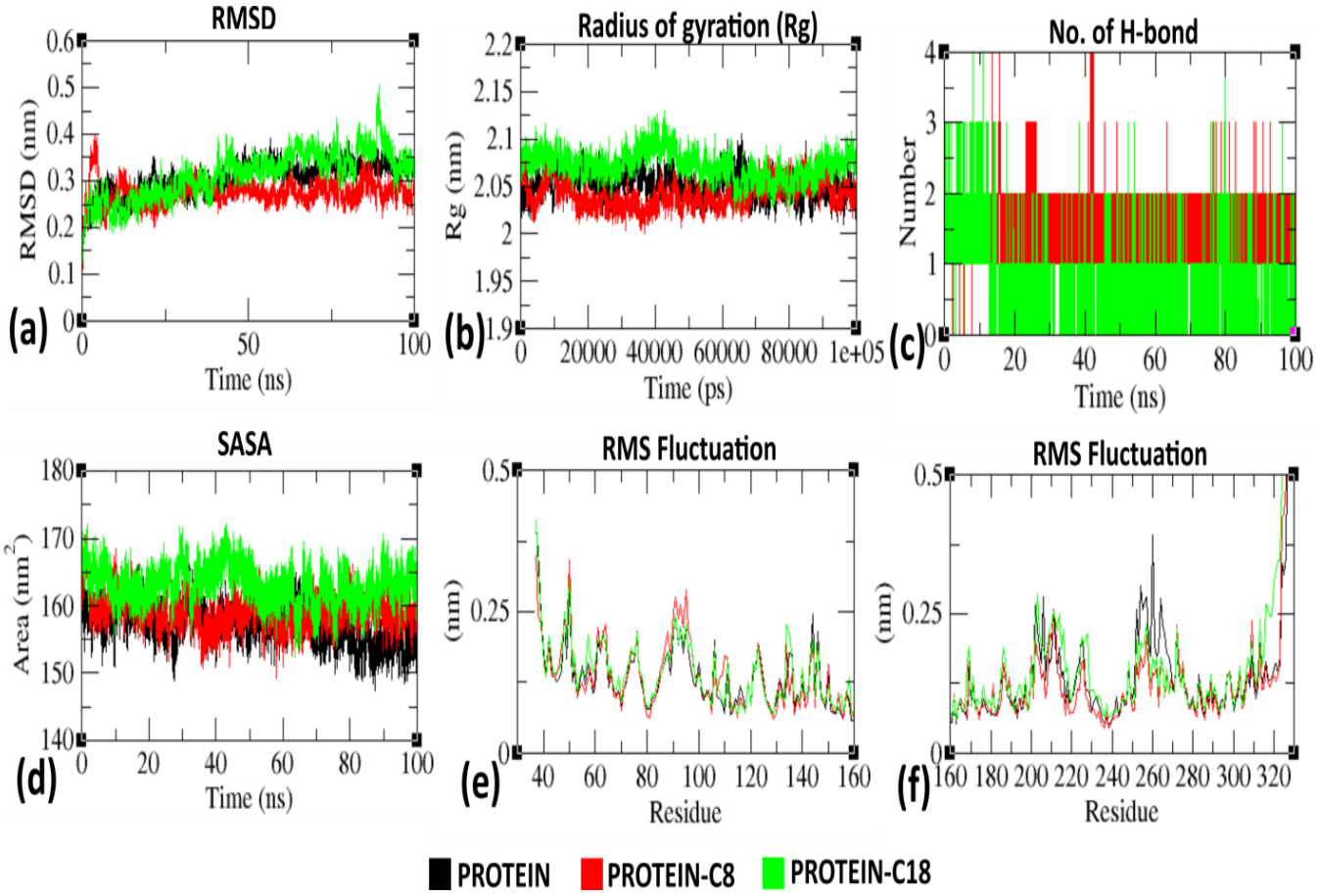

Figure 3. Analysis of MD simulation trajectories against the function of the RMSD, Rg, hydrogen bond, SASA, and RMSF of PLK1 (PDB ID: 2OWB) with synthetic compound **C8** and **C18** (ligand) complexes at 100,000 ps (100 ns). (**a**) RMSD; (**b**) radius of gyration (Rg); (**c**) hydrogen bonds; (**d**) SASA; (**e**,**f**) RMSF plot of the protein in the presence of **C8** and **C18**.

3.3. Cytotoxicity Analysis

Based on initial screening through molecular docking analysis and further confirmation of the stability of the PLK1 docked complex based on molecular dynamics, **C8** and **C18** appeared to be the most active compounds. Thus, the cytotoxicity of **C8** and **C18** was assessed against three cancer cell lines (A549, MCF 7, and HepG2) via MTT assays. As represented in Table 3 and Figure 4, compounds **C8** and **C18** exhibited significant inhibitory activities against A549 cells with IC_{50} values of 9.54 µM and 10.38 µM, respectively. However, the reference compound (doxorubicin) showed a better IC_{50} (8.20 µM) than the tested compounds. Moreover, the compounds **C8** and **C18** were tested on normal human lung epithelial BEAS-2B cells, and the IC_{50} values for both were found to be more than 200 µM. This showed a selectivity index of >10, which indicates that both **C8** and **C18** have more efficacy against tumor cells than the toxicity against normal cells. It can also be inferred from Table 2 that **C8** was more potent than **C18** against the tested cell lines. In addition, both **C8** and **C18** were less active against MCF7 and HepG2 cells than A549 cells. The lineage of A549 cells is the lung, MCF7 cells is the breast, and HepG2 cells is the liver; thus, the more potent activity of tested compounds against A549 cells has its due relevance.

There is a plethora of evidence that shows the correlation of tuberculosis with lung cancer, and tuberculosis is considered an important risk factor for lung cancer [48–50]. Hence, targeting lung cancer with anti-tubercular compound(s) seems to be an appealing strategy and could provide a boon to a tuberculosis-infected lung cancer patient in the future. Based on the cytotoxicity results, **C8** was selected further for cell cycle, cell apoptosis, and DAPI analysis against A549 cells to obtain deeper insight into the anticancer action.

Table 3. IC_{50} values of compounds against different tumor cell lines.

Compounds	IC_{50} (μM)		
	MCF7	**A549**	**HepG2**
C8	10.51 ± 1.9	9.54 ± 1.1	10.82 ± 1.3
C18	12.34 ± 0.9	10.38 ± 1.7	11.41 ± 2.5
Doxorubicin *	10.96 ± 1.6	8.20 ± 0.9	9.21 ± 1.0

* Doxorubicin was used as a positive control.

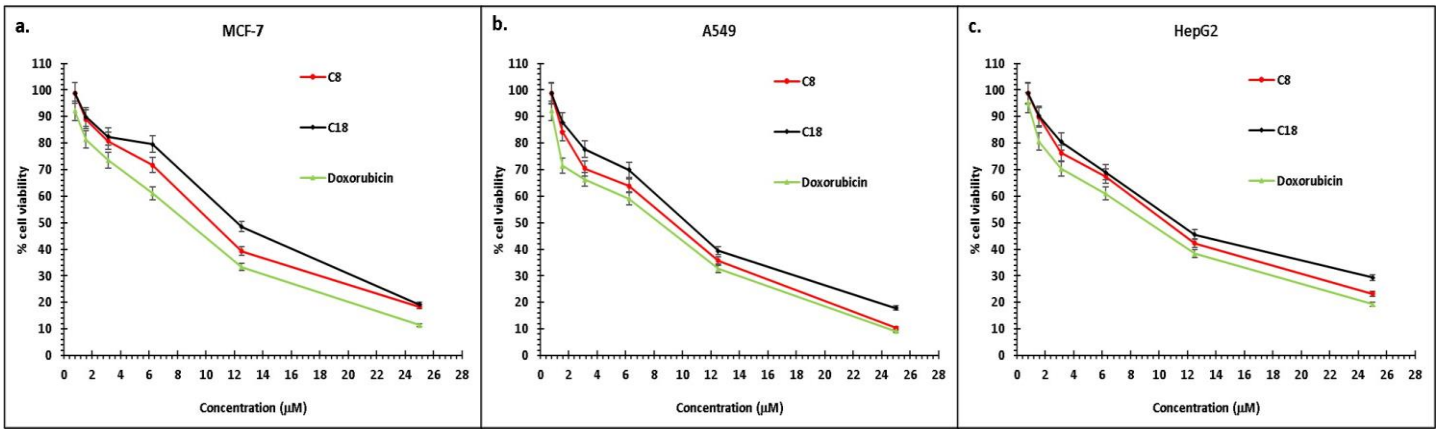

Figure 4. Cytotoxicity study of the test compounds **C8** and **C18** against MCF-7, A549, and HepG2 cells and their comparison with the positive control (doxorubicin). (**a**) Dose-response curve of test compounds for % cell viability against MCF-7 cell lines. (**b**) Dose-response curve of test compounds for % cell viability against A-549 cell lines. (**c**) Dose-response curve of test compounds for % cell viability against HepG2 cells.

3.4. Cell Cycle Analysis

Cell cycle arrest could be correlated well with the growth inhibition of cancer cells. Reports suggest that benzohydrazide derivatives stop cell progression at the G2/M phase of the cell cycle [51–53]. However, in the present study, to explain the action of **C8** on cell cycle distributions, A549 cells were treated with 10 μM (**C8**) for 24 h, and the distributions of A549 cells (treated and untreated) in various stages of the cell cycle were evaluated via flow cytometry (Figure 5). Consistent with the earlier findings [51–53], **C8** treatment led to maximum accumulation of A549 cells at the G2/M phase (39.48%); however, untreated A549 cells showed only 9.34% cells at the G2/M phase (Table 4). In addition, cell % was markedly reduced from 88.79% to 31.22% at G0/G1 phase when A549 cells were treated with **C8**. Obtained results suggested that **C8** demonstrated a significant antineoplastic effect and led to the stoppage A549 cell cycle progression at G2/M, metaphase, after the gestation period of 24 h. These results were in accordance with the other recent research conducted on A549 cells, wherein the anticancer effects were attributed to the blocking of the G2/M phase [54–56].

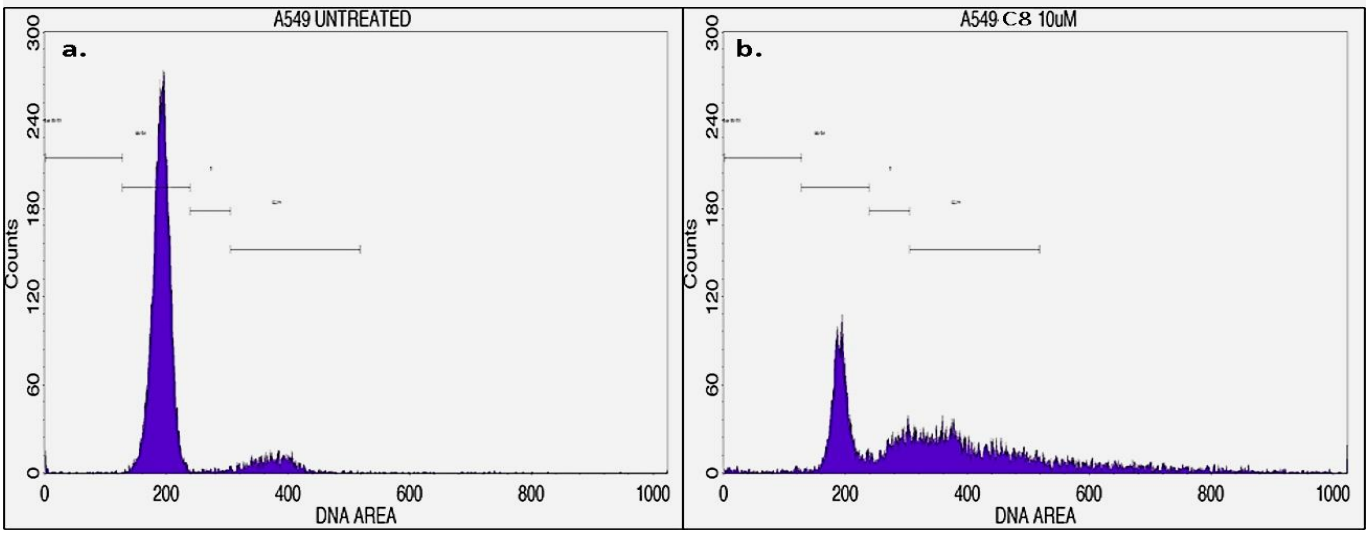

Figure 5. Flow cytometric histograms showing the phases of cell cycle distribution in the A549 cell line treated with (**a**) **C8** at a 10 µM concentration compared to the (**b**) untreated control.

Table 4. Effect of **C8** compound on cell cycle distributions of A549 cells.

Cell Cycle Stage	Untreated	C8 (10 µM)
Sub G0/G1	0.53	1.63
G0/G1	88.79	31.22
S	1.03	12.44
G2/M	9.34	39.48

3.5. Cell Apoptosis Analysis

To further understand the role of apoptosis in the anticancer properties of **C8**, FITC Annexin V/Propidium iodide staining was performed to evaluate the morphological changes upon treatment of A549 cells with **C8**. The quadrant plot (Figure 6) generated could distinguish live cells in the lower (left) quadrant (stained −ve for PI and FITC-annexin V), early apoptotic cells in the lower (right) quadrant (stained −ve for PI and +ve for FITC-annexin V), necrotic dead cells in the upper (left) quadrant (stained +ve for PI), and late apoptotic cells in the upper (right) quadrant (stained +ve for PI and FITC-annexin V). After treatment with **C8**, the percentage of apoptotic cells was moderately observed in early and late apoptotic states. The observations suggested that the test compound, **C8**, spurs reasonable apoptosis in human lung cancer A549 cells.

Figure 7 represents the bar graph for details of the percentage of cell stages observed in the quadrant layout in the apoptosis study. Here, the apoptosis rate was 33.21% (14.64% early apoptotic and 18.57% late apoptotic cells) in **C8**-treated A549 cells, whereas the percentage of viable cells was reduced from 99.88% to 60.52% after **C8** treatment of A549 cells, and 6.27% cells were reported as necrotic dead cells.

Moreover, Figure 8 shows the Annexin V histogram, obtained by using a BD FACS Calibur™ that differentiates cells at the M1 and M2 stages. Here, M1 denotes the negative expression/region, and M2 denotes the positive expression/region. The cells expressing Annexin V (M2 region) were considered apoptotic cells. Consequently, it can be concluded that the **C8** treatment of A549 cells triggered a shift in the cells towards apoptosis. Hence, it could be safely stated that **C8** not only arrested the G2/M stage of the cell cycle, but effectively induced apoptosis in A549 lung cancer cells.

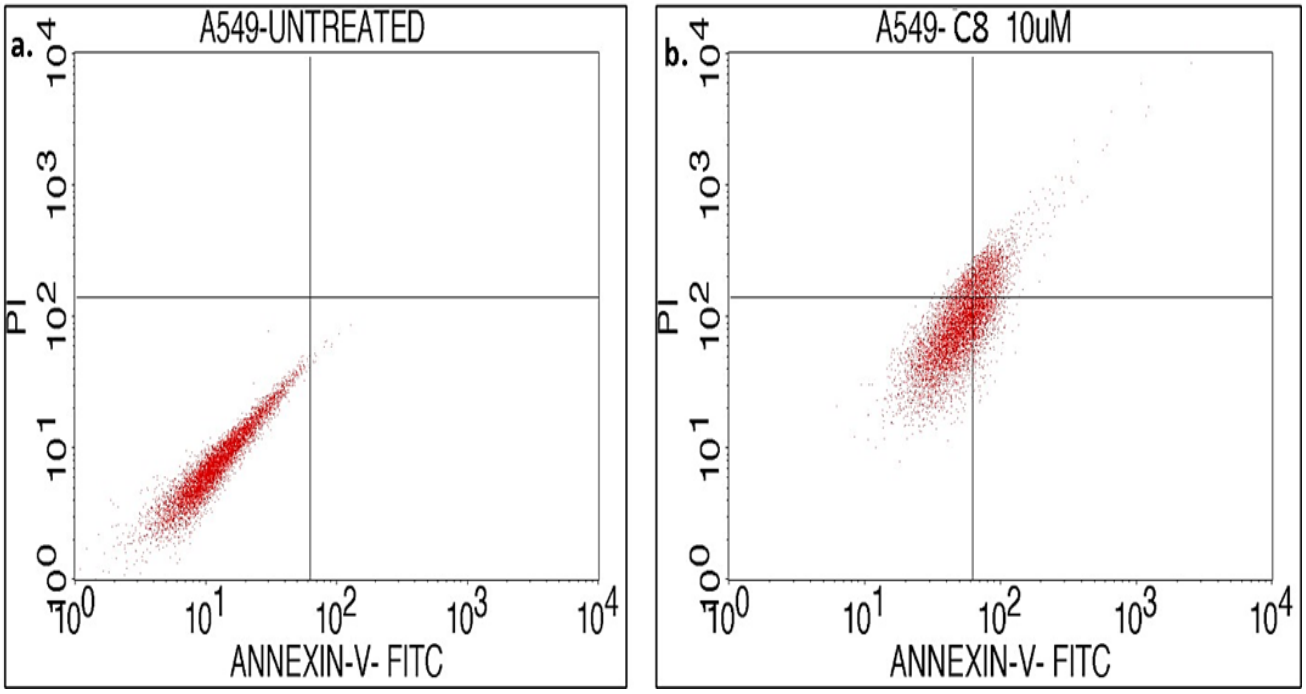

Figure 6. Quadrangular plot representing Annexin V/PI expression in A549 cells upon culture in the absence (**a**) and presence (**b**) of **C8** at a 10 μM concentration.

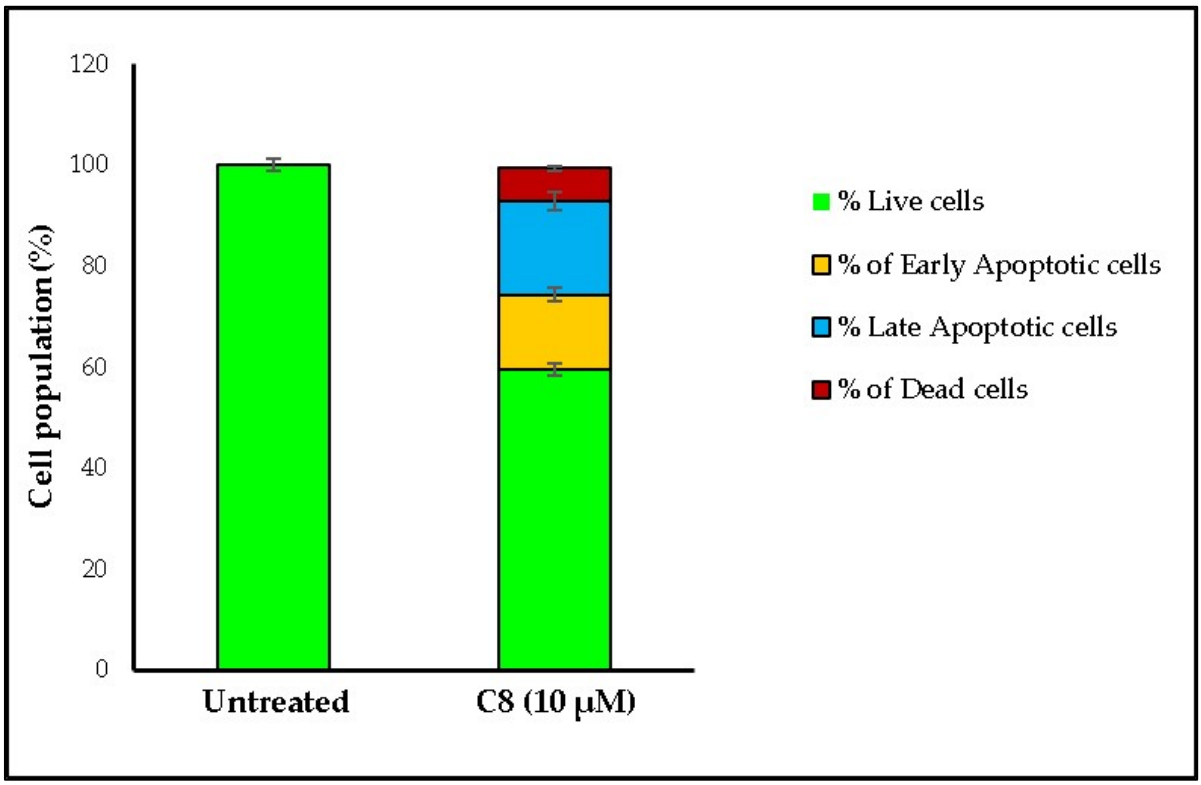

Figure 7. Bar graph showing the % of live, apoptotic, and dead cells in the absence and presence of **C8** at a 10 μM concentration.

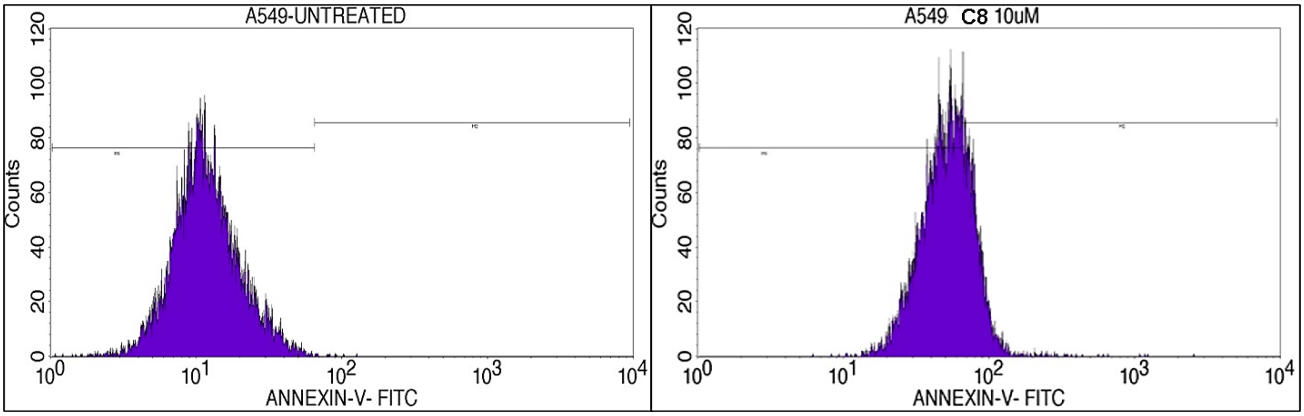

Figure 8. Histograms representing the Annexin V expression in A549 cells upon culture in the absence (**a**) and presence (**b**) of **C8** at a 10 µM concentration.

3.6. DAPI Assay

A DAPI staining assay was used to determine DNA fragmentation in **C8**-treated A549 lung cancer cells. Marked changes in the nuclear morphology and DNA fragmentation within the nucleus of the treated cells were observed (Figure 9). Here, cell nuclei were stained in blue, white arrows represent healthy DNA, and yellow arrows represent condensed and damaged DNA of the cells. In comparison to the untreated cells, **C8**-treated A549 cells showed significant DNA damage, blebbing, and condensing of the nucleus after the treatment period of 24 h; thus, confirming the DNA-damaging effect of **C8** against lung cancer A549 cells.

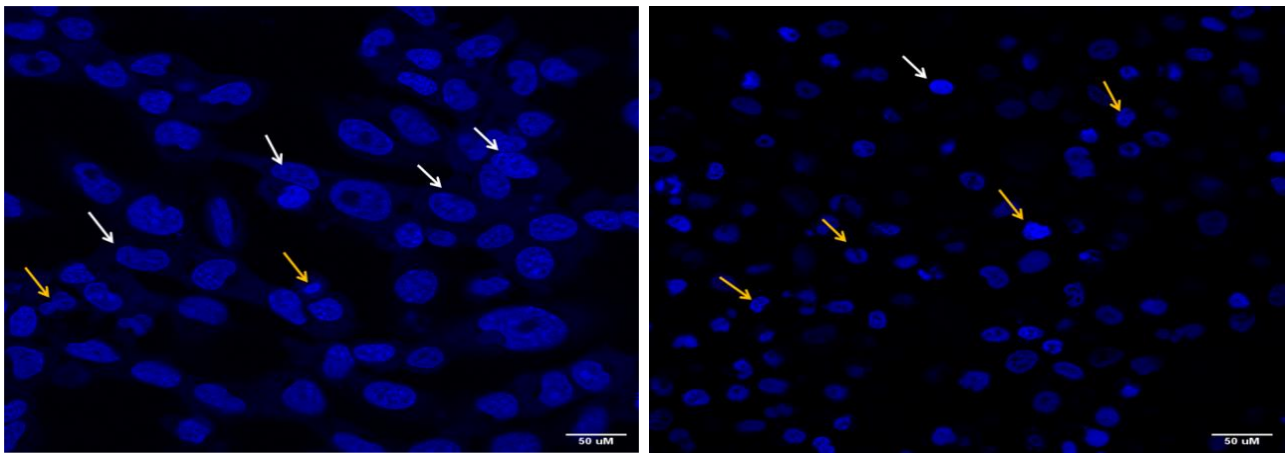

Figure 9. Fluorescent microscope images depicting the nuclear damage of DAPI-stained A549 cells at a magnification of 40×.

In the present investigation, compound **8** (**C8**) was found to be the most potent one among all the tested compounds during in silico screening against a cancer target (PLK1), which further showed a marked in vitro anticancer effect against A549 cell lines. Here, PLK1 was used as a biotarget for the initial screening of pyrrolyl benzohydrazide derivatives. In fact, PLK1 is overexpressed in different cancer cells [41–45] and plays an important role in mitosis initiation i.e., transition from G2 phase into the M phase [57]. The present study indicated that compound **C8**, screened on the basis of PLK1 inhibition and cell cytotoxicity, resulted in the marked arrest of A549 cells at the G2/M phase and induced apoptosis. In accordance with our findings, several earlier studies have also reported the cell cycle arrest of cancer cells at the DNA damage G2/M checkpoint and apoptosis after PLK1

inhibition [58–60]. In fact, strong PLK1 associations with the A549 cells [61–63] further strengthen the outcomes. However, it is too early to provide the conclusive remark on the applicability of **C8** as a dual therapeutic agent for tuberculosis and lung cancer. It is noteworthy to mention that the authors have already started to work on deciphering the exact molecular mechanism of the anticancer action and an in vivo evaluation of **C8**. Nevertheless, present outcomes might help in the development of new anti-cancer medications designed on anti-tubercular scaffolds, especially against lung cancer.

4. Conclusions

The present study evaluated the anti-cancer potential of anti-tubercular pyrrolyl benzohydrazide derivatives. The initial screening of different anti-tubercular pyrrolyl benzohydrazide derivatives was performed via computational approaches using docking and molecular dynamics studies. The compound N′-(4-(1H-pyrrol-1-yl) benzoyl)-3-chlorobenzohydrazide (named as **C8**) was screened out as the most potent one, among all the tested derivatives. However, an in vitro cytotoxicity assessment against cancer cell lines confirmed the computational findings. Further, to obtain insight into the anticancer activity of **C8** against human lung cancer A549 cells, cell cycle, apoptosis, and DAPI analyses were performed. Cell cycle and apoptosis analyses confirmed the arrest of the cell cycle at the G2/M phase and the induction of apoptosis in A549 cells after treatment with **C8**. Moreover, DAPI analysis confirmed the DNA fragmentation in **C8**-treated A549 cells. Still, more details of anti-cancer mechanistic aspects need to be studied along with in vivo assessments to bring these findings into reality. Nevertheless, an anti-tubercular compound showing potent anticancer potential, as well as against lung cancer, has its own due clinical relevance. This study might pave the way for a therapeutic strategy for tuberculosis-infected lung cancer patients in the near future.

Supplementary Materials: The following supporting information can be downloaded at: https://www.mdpi.com/article/10.3390/pr11071889/s1, Figure S1: Analysis of MD simulation trajectories against the functions of RMSD, Rg, hydrogen bond, SASA, and RMSF of PLK1 (PDB ID: 2OWB) with the control compound BI2536 (ligand) complex at 100000 ps (100 ns). (a) RMSD; (b) radius of gyration (Rg); (c) hydrogen bonds; (d) SASA; (e,f) RMSF plot of the protein in the presence of BI2536.

Author Contributions: Conceptualization, T.A.H., T.H. and A.M.; methodology, S.D. and N.V.G.; software, S.D., F.A. and S.M.D.R.; validation, S.D., N.V.G. and S.M.D.R.; formal analysis, F.A. and A.M.; resources, T.A.H. and A.M.; writing—original draft preparation, T.H., S.M.D.R. and N.V.G.; writing—review and editing, A.M., F.A. and T.A.H.; supervision, T.H. and T.A.H.; project administration, A.M. and T.A.H.; funding acquisition, T.A.H. All authors have read and agreed to the published version of the manuscript.

Funding: This research has been funded by a Scientific Research Deanship at the University of Ha'il—Saudi Arabia through project number BA-2102.

Institutional Review Board Statement: Not applicable.

Informed Consent Statement: Not applicable.

Data Availability Statement: Not applicable.

Acknowledgments: This research has been funded by a Scientific Research Deanship at the University of Ha'il—Saudi Arabia through project number BA-2102.

Conflicts of Interest: The authors declare no conflict of interest.

References

1. Albrecht, B.; Andersen, S.; Chauhan, K.; Graybosch, D.; Menu, P. Pursuing Breakthroughs in Cancer-Drug Development. Available online: https://www.mckinsey.com/industries/life-sciences/our-insights/pursuing-breakthroughs-in-cancer-drug-development (accessed on 25 January 2023).
2. Cancer. Available online: https://www.who.int/news-room/fact-sheets/detail/cancer (accessed on 25 January 2023).
3. Siegel, R.L.; Miller, K.D.; Wagle, N.S.; Jemal, A. Cancer Statistics, 2023. CA. *Cancer J. Clin.* **2023**, *73*, 17–48. [CrossRef] [PubMed]

4. Schein, C.H. Repurposing Approved Drugs for Cancer Therapy. *Br. Med. Bull.* **2021**, *137*, 13–27. [CrossRef]
5. Rodrigues, R.; Duarte, D.; Vale, N. Drug repurposing in cancer therapy: Influence of patient's genetic background in breast cancer treatment. *Int. J. Mol. Sci.* **2022**, *23*, 4280. [CrossRef] [PubMed]
6. Patil, S.M.; Sawant, S.S.; Kunda, N.K. Inhalable Bedaquiline-Loaded Cubosomes for the Treatment of Non-Small Cell Lung Cancer (NSCLC). *Int. J. Pharm.* **2021**, *607*, 121046. [CrossRef] [PubMed]
7. Parvathaneni, V.; Elbatanony, R.S.; Goyal, M.; Chavan, T.; Vega, N.; Kolluru, S.; Muth, A.; Gupta, V.; Kunda, N.K. Repurposing Bedaquiline for Effective Non-Small Cell Lung Cancer (NSCLC) Therapy as Inhalable Cyclodextrin-Based Molecular Inclusion Complexes. *Int. J. Mol. Sci.* **2021**, *22*, 4783. [CrossRef]
8. Choi, J.; Park, S.-J.; Jee, J.-G. Analogues of Ethionamide, a Drug Used for Multidrug-Resistant Tuberculosis, Exhibit Potent Inhibition of Tyrosinase. *Eur. J. Med. Chem.* **2015**, *106*, 157–166. [CrossRef] [PubMed]
9. Choi, J.; Jee, J.-G. Repositioning of Thiourea-Containing Drugs as Tyrosinase Inhibitors. *Int. J. Mol. Sci.* **2015**, *16*, 28534–28548. [CrossRef]
10. Falzon, D.; Hill, G.; Pal, S.N.; Suwankesawong, W.; Jaramillo, E. Pharmacovigilance and Tuberculosis: Applying the Lessons of Thioacetazone. *Bull. World Health Organ.* **2014**, *92*, 918–919. [CrossRef]
11. Lv, Q.; Wang, D.; Yang, Z.; Yang, J.; Zhang, R.; Yang, X.; Wang, M.; Wang, Y. Repurposing Antitubercular Agent Isoniazid for Treatment of Prostate Cancer. *Biomater. Sci.* **2019**, *7*, 296–306. [CrossRef]
12. Joshi, S.D.; Dixit, S.R.; Kulkarni, V.H.; Lherbet, C.; Nadagouda, M.N.; Aminabhavi, T.M. Synthesis, Biological Evaluation and in Silico Molecular Modeling of Pyrrolyl Benzohydrazide Derivatives as Enoyl ACP Reductase Inhibitors. *Eur. J. Med. Chem.* **2017**, *126*, 286–297. [CrossRef]
13. Wang, H.C.; Yan, X.Q.; Yan, T.L.; Li, H.X.; Wang, Z.C.; Zhu, H.L. Design, synthesis and biological evaluation of benzohydrazide derivatives containing dihydropyrazoles as potential EGFR kinase inhibitors. *Molecules.* **2016**, *21*, 1012. [CrossRef] [PubMed]
14. Basha, N.J.; Basavarajaiah, S.M.; Shyamsunder, K. Therapeutic Potential of Pyrrole and Pyrrolidine Analogs: An Update. *Mol. Divers.* **2022**, *26*, 2915–2937. [CrossRef]
15. Mateev, E.; Georgieva, M.; Zlatkov, A. Pyrrole as an Important Scaffold of Anticancer Drugs: Recent Advances. *J. Pharm. Pharm. Sci.* **2022**, *25*, 24–40. [CrossRef] [PubMed]
16. Tarzia, G.; Duranti, A.; Tontini, A.; Spadoni, G.; Mor, M.; Rivara, S.; Plazzi, P.V.; Kathuria, S.; Piomelli, D. Synthesis and Structure–Activity Relationships of a Series of Pyrrole Cannabinoid Receptor Agonists. *Bioorg. Med. Chem.* **2003**, *11*, 3965–3973. [CrossRef] [PubMed]
17. Chauhan, M.; Kumar, R. Medicinal Attributes of Pyrazolo[3,4-d]Pyrimidines: A Review. *Bioorg. Med. Chem.* **2013**, *21*, 5657–5668. [CrossRef]
18. Ansari, A.; Ali, A.; Asif, M.; Shamsuzzaman, S. Review: Biologically Active Pyrazole Derivatives. *New J. Chem.* **2017**, *41*, 16–41. [CrossRef]
19. Saleh, N.M.; El-Gazzar, M.G.; Aly, H.M.; Othman, R.A. Novel Anticancer Fused Pyrazole Deriv Biologically active pyrazole derivatives atives as EGFR and VEGFR-2 Dual TK Inhibitors. *Front. Chem.* **2020**, *7*, 917. [CrossRef]
20. Arjun, H.A.; Elancheran, R.; Manikandan, N.; Lakshmithendral, K.; Ramanathan, M.; Bhattacharjee, A.; Lokanath, N.K.; Kabilan, S. Design, Synthesis, and Biological Evaluation of (E)-N′-((1-Chloro-3,4-Dihydronaphthalen-2-Yl)Methylene)Benzohydrazide Derivatives as Anti-Prostate Cancer Agents. *Front. Chem.* **2019**, *7*, 474. [CrossRef]
21. Morcoss, M.; Abdelhafez, E.S.; Abdel-Rahman, H.; Abdel-Aziz, M.; El-Ella, D.A. Novel Benzimidazole/Hydrazone Derivatives as Promising Anticancer Lead Compounds: Design, Synthesis, and Molecular Docking Study. *J. Adv. Biomed. Pharm. Sci.* **2020**, *3*, 45–52. [CrossRef]
22. Sarno, F.; Papulino, C.; Franci, G.; Andersen, J.H.; Cautain, B.; Melardo, C.; Altucci, L.; Nebbioso, A. 3-Chloro-N′-(2-Hydroxybenzylidene) Benzohydrazide: An LSD1-Selective Inhibitor and Iron-Chelating Agent for Anticancer Therapy. *Front. Pharmacol.* **2018**, *9*, 1006. [CrossRef]
23. Ohira, M.; Iwasaki, Y.; Tanaka, C.; Kuroki, M.; Matsuo, N.; Kitamura, T.; Yukuhiro, M.; Morimoto, H.; Pang, N.; Liu, B.; et al. A Novel Anti-Microtubule Agent with Carbazole and Benzohydrazide Structures Suppresses Tumor Cell Growth in Vivo. *Biochim. Biophys. Acta-Gen. Subj.* **2015**, *1850*, 1676–1684. [CrossRef]
24. Kamath, P.R.; Sunil, D.; Ajees, A.A.; Pai, K.S.R.; Biswas, S. N′-((2-(6-Bromo-2-Oxo-2H-Chromen-3-Yl)-1H-Indol-3-Yl)Methylene) Benzohydrazide as a Probable Bcl-2/Bcl-XL Inhibitor with Apoptotic and Anti-Metastatic Potential. *Eur. J. Med. Chem.* **2016**, *120*, 134–147. [CrossRef]
25. Radwan, A.A.; Al-Mohanna, F.; Alanazi, F.K.; Manogaran, P.S.; Al-Dhfyan, A. Target β-Catenin/CD44/Nanog Axis in Colon Cancer Cells by Certain N′-(2-Oxoindolin-3-Ylidene)-2-(Benzyloxy)Benzohydrazides. *Bioorg. Med. Chem. Lett.* **2016**, *26*, 1664–1670. [CrossRef]
26. O'Boyle, N.M.; Banck, M.; James, C.A.; Morley, C.; Vandermeersch, T.; Hutchison, G.R. Open Babel: An Open Chemical Toolbox. *J. Cheminform.* **2011**, *3*, 33. [CrossRef]
27. Rizvi, S.M.D.; Shakil, S.; Haneef, M. A Simple Click by Click Protocol to Perform Docking: AutoDock 4.2 Made Easy for Non-Bioinformaticians. *EXCLI J.* **2013**, *12*, 831–857.
28. Trott, O.; Olson, A.J. AutoDock Vina: Improving the Speed and Accuracy of Docking with a New Scoring Function, Efficient Optimization, and Multithreading. *J. Comput. Chem.* **2009**, *31*, 455–461. [CrossRef] [PubMed]

29. Rizvi, S.M.D.; Alshammari, A.A.A.; Almawkaa, W.A.; Ahmed, A.B.F.; Katamesh, A.; Alafnan, A.; Almutairi, T.J.; Alshammari, R.F. An Oncoinformatics Study to Predict the Inhibitory Potential of Recent FDA-Approved Anti-Cancer Drugs against Human Polo-like Kinase 1 Enzyme: A Step towards Dual-Target Cancer Medication. *3 Biotech* **2019**, *9*, 70. [CrossRef] [PubMed]
30. Hess, B.; Kutzner, C.; van der Spoel, D.; Lindahl, E. GROMACS 4: Algorithms for Highly Efficient, Load-Balanced, and Scalable Molecular Simulation. *J. Chem. Theory Comput.* **2008**, *4*, 435–447. [CrossRef] [PubMed]
31. Bjelkmar, P.; Larsson, P.; Cuendet, M.A.; Hess, B.; Lindahl, E. Implementation of the CHARMM Force Field in GROMACS: Analysis of Protein Stability Effects from Correction Maps, Virtual Interaction Sites, and Water Models. *J. Chem. Theory Comput.* **2010**, *6*, 459–466. [CrossRef] [PubMed]
32. Zoete, V.; Cuendet, M.A.; Grosdidier, A.; Michielin, O. SwissParam: A Fast Force Field Generation Tool for Small Organic Molecules. *J. Comput. Chem.* **2011**, *32*, 2359–2368. [CrossRef]
33. Mark, P.; Nilsson, L. Structure and dynamics of the TIP3P, SPC, and SPC/E water models at 298 K. *J. Phys. Chem. A.* **2001**, *105*, 9954–9960. [CrossRef]
34. Mandal, S.P.; Garg, A.; Prabitha, P.; Wadhwani, A.D.; Adhikary, L.; Kumar, B.R.P. Novel Glitazones as PPARγ Agonists: Molecular Design, Synthesis, Glucose Uptake Activity and 3D QSAR Studies. *Chem. Cent. J.* **2018**, *12*, 141. [CrossRef] [PubMed]
35. Murthy, S.S.; Narsaiah, T.B. Cytotoxic Effect of Bromelain on HepG2 Hepatocellular Carcinoma Cell Line. *Appl. Biochem. Biotechnol.* **2021**, *193*, 1873–1897. [CrossRef] [PubMed]
36. Crowley, L.C.; Chojnowski, G.; Waterhouse, N.J. Measuring the DNA content of cells in apoptosis and at different cell-cycle stages by propidium iodide staining and flow cytometry. *Cold Spring Harb. Protoc.* **2016**, *2016*, pdb-rot087247. [CrossRef] [PubMed]
37. Andree, H.A.; Reutelingsperger, C.P.; Hauptmann, R.; Hemker, H.C.; Hermens, W.T.; Willems, G.M. Binding of Vascular Anticoagulant Alpha (VAC Alpha) to Planar Phospholipid Bilayers. *J. Biol. Chem.* **1990**, *265*, 4923–4928. [CrossRef]
38. Hotz, M.A.; Gong, J.; Traganos, F.; Darzynkiewicz, Z. Flow Cytometric Detection of Apoptosis: Comparison of the Assays of in Situ DNA Degradation and Chromatin Changes. *Cytometry* **1994**, *15*, 237–244. [CrossRef]
39. Talevi, A.; Bellera, C.L. Challenges and Opportunities with Drug Repurposing: Finding Strategies to Find Alternative Uses of Therapeutics. *Expert Opin. Drug Discov.* **2020**, *15*, 397–401. [CrossRef]
40. Drug Repurposing Market-Global Market Share, Trends, Analysis and Forecast, 2023–2032. Available online: https://www.insightslice.com/drug-repurposing-market#:~:text=The%20global%20drug%20repurposing%20market,therapeutical%20uses%20for%20existing%20drugs (accessed on 7 February 2023).
41. Shakil, S.; Baig, M.H.; Tabrez, S.; Rizvi, S.M.D.; Zaidi, S.K.; Ashraf, G.M.; Ansari, S.A.; Khan, A.A.P.; Al-Qahtani, M.H.; Abuzenadah, A.M.; et al. Molecular and Enzoinformatics Perspectives of Targeting Polo-like Kinase 1 in Cancer Therapy. *Semin. Cancer Biol.* **2019**, *56*, 47–55. [CrossRef]
42. Cholewa, B.D.; Liu, X.; Ahmad, N. The Role of Polo-like Kinase 1 in Carcinogenesis: Cause or Consequence? *Cancer Res.* **2013**, *73*, 6848–6855. [CrossRef]
43. Chiappa, M.; Petrella, S.; Damia, G.; Broggini, M.; Guffanti, F.; Ricci, F. Present and Future Perspective on PLK1 Inhibition in Cancer Treatment. *Front. Oncol.* **2022**, *12*, 903016. [CrossRef]
44. Su, S.; Chhabra, G.; Singh, C.K.; Ndiaye, M.A.; Ahmad, N. PLK1 Inhibition-Based Combination Therapies for Cancer Management. *Transl. Oncol.* **2022**, *16*, 101332. [CrossRef] [PubMed]
45. Gutteridge, R.E.A.; Ndiaye, M.A.; Liu, X.; Ahmad, N. Plk1 Inhibitors in Cancer Therapy: From Laboratory to Clinics. *Mol. Cancer Ther.* **2016**, *15*, 1427–1435. [CrossRef] [PubMed]
46. Kothe, M.; Kohls, D.; Low, S.; Coli, R.; Cheng, A.C.; Jacques, S.L.; Johnson, T.L.; Lewis, C.; Loh, C.; Nonomiya, J.; et al. Structure of the Catalytic Domain of Human Polo-like Kinase 1. *Biochemistry* **2007**, *46*, 5960–5971. [CrossRef]
47. Liang, H.; Liu, H.; Kuang, Y.; Chen, L.; Ye, M.; Lai, L. Discovery of Targeted Covalent Natural Products against PLK1 by Herb-Based Screening. *J. Chem. Inf. Model.* **2020**, *60*, 4350–4358. [CrossRef] [PubMed]
48. Keikha, M.; Esfahani, B. The Relationship between Tuberculosis and Lung Cancer. *Adv. Biomed. Res.* **2018**, *7*, 58. [CrossRef]
49. Cabrera-Sanchez, J.; Cuba, V.; Vega, V.; van der Stuyft, P.; Otero, L. Lung Cancer Occurrence after an Episode of Tuberculosis: A Systematic Review and Meta-Analysis. *Eur. Respir. Rev.* **2022**, *31*, 220025. [CrossRef]
50. Qin, Y.; Chen, Y.; Chen, J.; Xu, K.; Xu, F.; Shi, J. The Relationship between Previous Pulmonary Tuberculosis and Risk of Lung Cancer in the Future. *Infect. Agent. Cancer* **2022**, *17*, 20. [CrossRef]
51. Fujita, M.; Oshima, T.; Morimoto, H. Benzohydrazide Derivative for Inducing g2/m Phase Arrest and Cell Death. Patent No WO2013061669A1, 2 May 2013.
52. Wang, G.; He, M.; Liu, W.; Fan, M.; Li, Y.; Peng, Z. Design, synthesis and biological evaluation of novel 2-phenyl-4,5,6,7-tetrahydro-1H- indole derivatives as potential anticancer agents and tubulin polymerization inhibitors. *Arab. J. Chem.* **2022**, *15*, 103504. [CrossRef]
53. Parrino, B.; Ullo, S.; Attanzio, A.; Spanò, V.; Cascioferro, S.; Montalbano, A.; Barraja, P.; Tesoriere, L.; Cirrincione, G.; Diana, P. New Tripentone Analogs with Antiproliferative Activity. *Molecules* **2017**, *22*, 2005. [CrossRef]
54. Zhang, Y.; Zhang, R.; Ni, H. Eriodictyol Exerts Potent Anticancer Activity against A549 Human Lung Cancer Cell Line by Inducing Mitochondrial-Mediated Apoptosis, G2/M Cell Cycle Arrest Vorinostat enhances the therapeutic potential of Erlotinib via MAPK in lung cancer cells and Inhibition of m-TOR/PI3K/Akt Signalling Pathway. *Arch. Med. Sci.* **2019**, *16*, 446–452. [CrossRef]

55. Song, Z.; Yin, Y.; Hao, S.; Wei, J.; Liu, B.; Huang, X.; Gao, C.; Zhu, R.; Liao, W.; Cai, D. JS-K induces G2/M phase cell cycle arrest and apoptosis in A549 and H460 cells via the p53/p21WAF1/CIP1 and p27KIP1 pathways. *Oncol. Rep.* **2019**, *41*, 3475–3487. [CrossRef]
56. Alqosaibi, A.I.; Abdel-Ghany, S.; Al-Mulhim, F.; Sabit, H. Vorinostat Enhances the Therapeutic Potential of Erlotinib via MAPK in Lung Cancer Cells. *Cancer Treat. Res. Commun.* **2022**, *30*, 100509. [CrossRef]
57. Liu, Z.; Sun, Q.; Wang, X. PLK1, a potential target for cancer therapy. *Transl. Oncol.* **2017**, *10*, 22–32. [CrossRef] [PubMed]
58. Schmit, T.L.; Zhong, W.; Setaluri, V.; Spiegelman, V.S.; Ahmad, N. Targeted depletion of Polo-like kinase (Plk) 1 through lentiviral shRNA or a small-molecule inhibitor causes mitotic catastrophe and induction of apoptosis in human melanoma cells. *J. Investig. Dermatol.* **2009**, *129*, 2843–2853. [CrossRef] [PubMed]
59. Jung, Y.; Kraikivski, P.; Shafiekhani, S.; Terhune, S.S.; Dash, R.K. Crosstalk between Plk1, p53, cell cycle, and G2/M DNA damage checkpoint regulation in cancer: Computational modeling and analysis. *Npj Syst. Biol. Appl.* **2021**, *7*, 46. [CrossRef] [PubMed]
60. Pezuk, J.A.; Brassesco, M.S.; Morales, A.G.; de Oliveira, J.C.; de Oliveira, H.F.; Scrideli, C.A.; Tone, L.G. Inhibition of polo-like kinase 1 induces cell cycle arrest and sensitizes glioblastoma cells to ionizing radiation. *Cancer Biother. Radiopharm.* **2013**, *28*, 516–522. [CrossRef] [PubMed]
61. Yan, W.; Yu, H.; Li, W.; Li, F.; Wang, S.; Yu, N.; Jiang, Q. Plk1 promotes the migration of human lung adenocarcinoma epithelial cells via STAT3 signaling. *Oncol. Lett.* **2018**, *16*, 6801–6807. [CrossRef] [PubMed]
62. Gunasekaran, P.; Lee, G.H.; Hwang, Y.S.; Koo, B.C.; Han, E.H.; Bang, G.; La, Y.K.; Park, S.; Kim, H.N.; Kim, M.H.; et al. An investigation of Plk1 PBD inhibitor KBJK557 as a tumor growth suppressor in non-small cell lung cancer. *J. Anal. Sci. Technol.* **2022**, *13*, 1–10. [CrossRef]
63. Zhang, R.; Xu, Z.; Ning, F.; Kong, Y.; Li, X.; Wang, X.; Yu, X. The effect of inhibition of Plk1 expression on the sensitivity and metastasis of cisplatin in lung cancer cell line A549. *Acta Med. Mediterr.* **2020**, *36*, 2833–2838.